



# Flexible liquid-diode microtubes from multimodal microfluidics

Chaoyu Yang<sup>a,b,c</sup> Wenzhao Li<sup>a,b</sup> Yuanjin Zhao<sup>a,b,1</sup> and Luoran Shang<sup>a,d,1</sup>

Edited by Todd M. Squires, University of California, Santa Barbara, CA; received February 8, 2024; accepted June 4, 2024 by Editorial Board Member Pablo G. Debenedetti

Directional transport of liquids is of great importance in energy saving, chemical/biomedical engineering, and microfluidics applications. Despite considerable progress in engineering different open surfaces to achieve liquid manipulation, the realization of diode-like liquid transport in enclosed spaces is still challenging. Here, a flexible diode microtube is presented for directional liquid transport within confined spaces using pulsed microfluidics. The microtubes exhibit sophisticated microstructures on the inner wall, replicated from a precisely controlled flow configuration in the microfluidic channel. Under the effect of asymmetric pinning and unbalanced Laplace pressure, such microtubes enable directional liquid transport in closed channels. More importantly, by integrating *in situ* flow lithography with the microfluidic system, segmented liquid diodes are fabricated as assembly units for the construction of fluidic–electronic circuits that perform logic operations. These results demonstrate the capacity of the present liquid-diode microtubes for flexible, directional, and programmable liquid transport. We believe that it can open an avenue for designing advanced fluidic circuit-based devices toward versatile practical applications.

bioinspired | microfluidics | liquid-diode microtube | directional liquid transport

Diodes are basic electronic components with two terminals having asymmetric electrical resistance that enable current flow in one direction (1). Advanced fabrication techniques enable packaging of integrated circuits in an encasement to protect the circuit from corrosion or damage (2). Analogous to the essential role of directional current flow in electronic circuits, directional flow of liquids is also a fundamental requirement for many chemical, biomedical, and environmental engineering fields as well as relevant industrial applications (3–12). In view of this, numerous efforts have been devoted to realizing directional liquid transport by leveraging wettability gradients (13–17), topographical gradients (4, 18–26), or their interplay (27–30) to provide unbalanced forces for liquid driving. Despite many achievements, the above working principles have been mostly implemented on open surfaces (6, 25, 31, 32), while directional liquid transport in closed spaces remains challenging, probably due to the complexities in manufacturing (33–35). Moreover, the current liquid transport surfaces are hardly reconfigurable, making it difficult to construct integrated three-dimensional (3D) systems toward more broad flow control applications.

Here, we present flexible liquid-diode microtubes from microfluidics for directional liquid transport in closed spaces, as shown in Fig. 1A. A coflow microfluidic spinning system is coupled with a programmable pulsation vibrator. Under precise control of the flow configuration and rational choice of the fluidic component, this system enables manufacturing of hollow microtubes with a round outer wall and a desired anisotropic inner wall. The inner wall is characterized by periodic microcorrugations, forming overlapped truncated cone-shaped cavities, each presenting a sharp edge and corner along the axial direction of the tube. Such sophisticated anisotropic structure provides unbalanced Laplace pressure as the driving force for directional transporting of diverse liquids within closed channels, making the microtubes liquid diodes (Fig. 1B). In addition, the exceptional flexibility of the liquid-diode microtubes allows for operation across arbitrary curved paths. Moreover, by integrating *in situ* flow lithography modality with the microfluidic system, it offers an efficient approach for fabricating segment liquid diodes, akin to electronic diode components. This allows for the construction of a fluidic–electronic circuit to achieve logic control. With these results, we believe that the present liquid diodes can find broad applications in liquid transport, and the multimodal microfluidic system opens an avenue for creating materials with unique anisotropic structures.

## Results

The principle of preparing the liquid-diode microtube lies in the formation of a corrugated core stream surrounded by a sheath stream in an active microfluidic platform (*SI Appendix*,

## Significance

Directional liquid transport within closed spaces is crucial for both fundamental studies and industrial applications. Despite extensive progress in engineering diverse open surfaces to guide liquid transport, the implementation of diode-like liquid transport in closed spaces is still challenging. In this study, we present a flexible liquid-diode microtube designed specifically for directional liquid transport in closed spaces, achieved through microfluidics. Additionally, a flow lithography modality is introduced to produce short microtube segments to construct a fluidic–electronic circuit with the ability to execute dual logic control.

Author affiliations: <sup>a</sup>Department of Rheumatology and Immunology, Nanjing Drum Tower Hospital, School of Biological Science and Medical Engineering, Southeast University, Nanjing 210096, China; <sup>b</sup>Oujiang Laboratory (Zhejiang Lab for Regenerative Medicine, Vision and Brain Health), Wenzhou Institute, University of Chinese Academy of Sciences, Wenzhou 325001, China; <sup>c</sup>Department of Mechanical and Automation Engineering, The Chinese University of Hong Kong, Hong Kong 999077, China; and <sup>d</sup>Shanghai Xuhui Central Hospital, Zhongshan-Xuhui Hospital, the Shanghai Key Laboratory of Medical Epigenetics, the International Co-Laboratory of Medical Epigenetics and Metabolism (Ministry of Science and Technology), Institutes of Biomedical Sciences, Fudan University, Shanghai 200032, China

Author contributions: C.Y., L.S., and Y.Z. conceived the concept; C.Y. designed the research; C.Y. and W.L. performed research; C.Y. contributed new reagents/analytic tools; C.Y. and L.S. analyzed data; and C.Y., L.S., and Y.Z. wrote the paper.

The authors declare no competing interest.

This article is a PNAS Direct Submission. T.M.S. is a guest editor invited by the Editorial Board.

Copyright © 2024 the Author(s). Published by PNAS. This article is distributed under [Creative Commons Attribution-NonCommercial-NoDerivatives License 4.0 \(CC BY-NC-ND\)](#).

<sup>1</sup>To whom correspondence may be addressed. Email: yjzhao@seu.edu.cn or luoranshang@fudan.edu.cn.

This article contains supporting information online at <https://www.pnas.org/lookup/suppl/doi:10.1073/pnas.2402331121/-DCSupplemental>.

Published July 3, 2024.

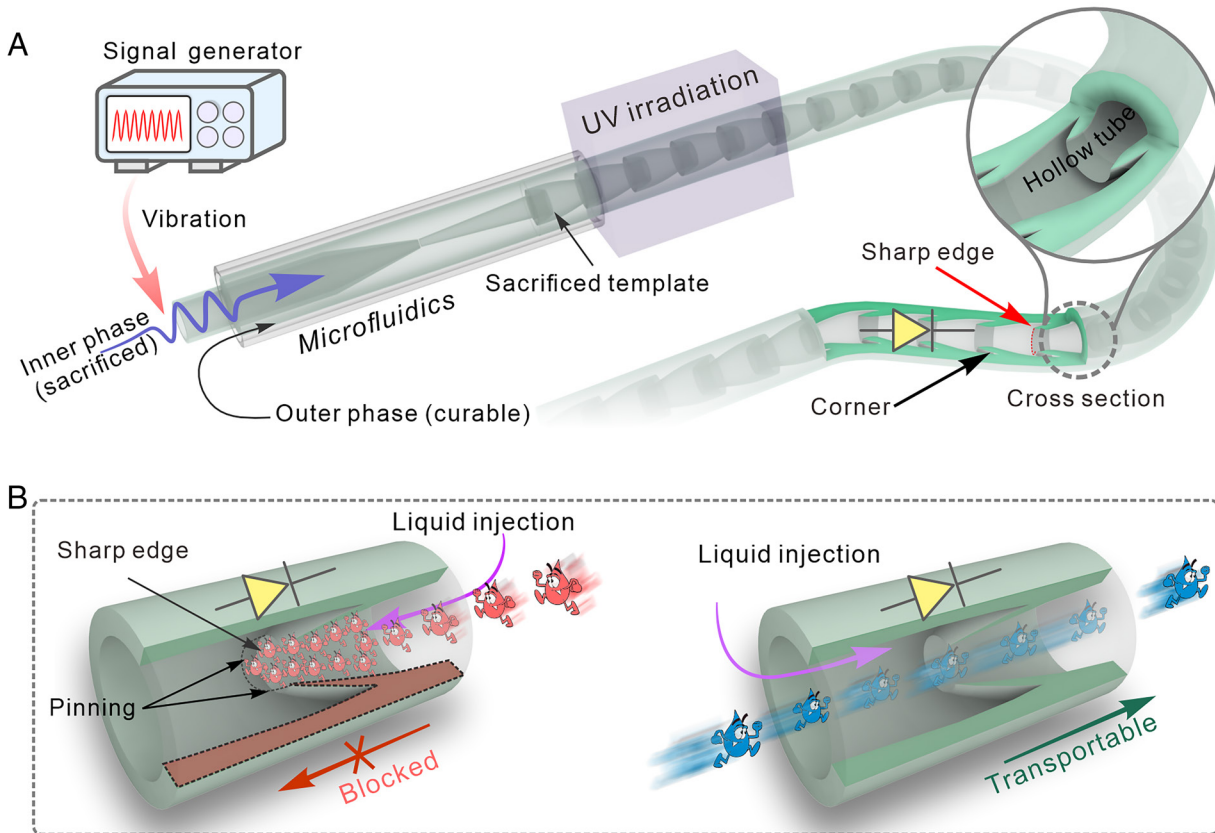


**Fig. 1.** Schematic illustrations of the generation and properties of the liquid-diode microtube. (*A*) Schematic illustration of the generation process of the liquid-diode microtube with an anisotropic-shaped inner wall by microfluidic spinning under periodic fluidic vibration. By introducing piezoelectric vibration, the inner stream is activated and deformed into corrugations. The outer phase is then polymerized by UV irradiation to generate the microtube. The core stream serves as a sacrificed layer, leaving the inner wall of the tube an inverse structure of the corrugations, forming overlapped truncated cone-shaped cavities, each presenting a sharp edge and corner along the axial direction of the tube. (*B*) Schematic of the directional liquid transport principle of the liquid-diode microtube. Liquid within the tube flows unidirectionally in the direction of the inverse truncated cone, while in the opposite bias, the sharp edge acts as a barrier, blocking flow in the other direction.

(*Fig. S1*). Microfluidics is a technique that enables precise and systematic processing of individual fluids in microscale channels (36–43). The coflow configuration is a widely explored regime in microfluidics for continuous spinning of microfibers (30, 44–49). Here, in this study, an active microfluidic spinning method is implemented to generate hollow microfibers, i.e., microtubes, with desired internal structures. In a typical experiment, the core stream fluid is a mixed solution of PVA and NaCl and the sheath stream fluid is a mixed solution of PEGDA and sodium alginate. By introducing piezoelectric vibration, the inner stream is activated and deformed into corrugations, as illustrated in Fig. 1*A*. We perform numerical simulations to track the evolution of the fluid–fluid interface. It reveals that the deformation is a result of the expansion and contraction of the core stream. The protruding segment transforms into a corrugated shape due to the parabolic velocity profile of the Poiseuille flow in the tube (Fig. 2*A* and *SI Appendix*, Fig. S2); the generation frequency of the corrugations directly corresponds to the piezoelectric frequency (*SI Appendix*, Fig. S3). Then, the fluids flow out of the tube and enter a collection solution containing  $\text{Ca}^{2+}$ , causing rapid cross-linking at the interface due to the presence of sodium alginate in the outer phase solution. (*SI Appendix*, Fig. S4). At this stage, the velocity profile becomes uniform (Fig. 2*A* and *B*) and the corrugated shape of the core stream remains unchanged for a long distance toward downstream (Fig. 2*C* and *Movie S1*).

As the flow streams enter the collection solution and form a thin ionic-cross-linked outer layer, they still have a certain degree of fluidity and continuously move downward. Additionally, by

adjusting the salinity of the inner fluid and the collection solution to control their densities (*SI Appendix*, Table S3), the diameter of the microtube,  $D$ , can be directly associated to the densities of the collection bath solution and the inner phase fluid, as shown in Fig. 2*D* and *E* and *SI Appendix*, Fig. S5 and Tables S1 and S2 and Note S1. It is worth noting that the concentration of the collection solution should not be too large, or it will cause an unstable state. For a typical experiment, by adjusting the concentration of the solutions used,  $D$  can be maintained the same as  $D_o$ , the inner diameter of the outer capillary (Fig. 2*C*). The average diameter of the core stream in the tube  $d_{in}$  and out in the collection solution  $d_{out}$  can be adjusted by the ratio of the inner ( $Q_i$ ) and outer ( $Q_o$ ) flow rate (50, 51) (details see *SI Appendix*, Note S2):

$$d_{in} = D_o \sqrt{\frac{\sqrt{1 + \frac{Q_i \eta_i}{Q_o \eta_o}} - \left(1 + \frac{Q_i}{Q_o}\right)}{\frac{\eta_i}{\eta_o} - 2 - \frac{Q_i}{Q_o}}}; d_{out} = D_o \sqrt{\frac{Q_i}{Q_i + Q_o}}, [1]$$

where  $\eta_i$  and  $\eta_o$  are the viscosities of the inner stream and outer sheath, respectively. In addition, the pitch ( $p$ ) of the corrugation of the core stream (in the collection solution) can be programmed by the piezoelectric frequency ( $f_p$ ):

$$p = \frac{4(Q_i + Q_o)}{\pi f_p D_o^2}. [2]$$

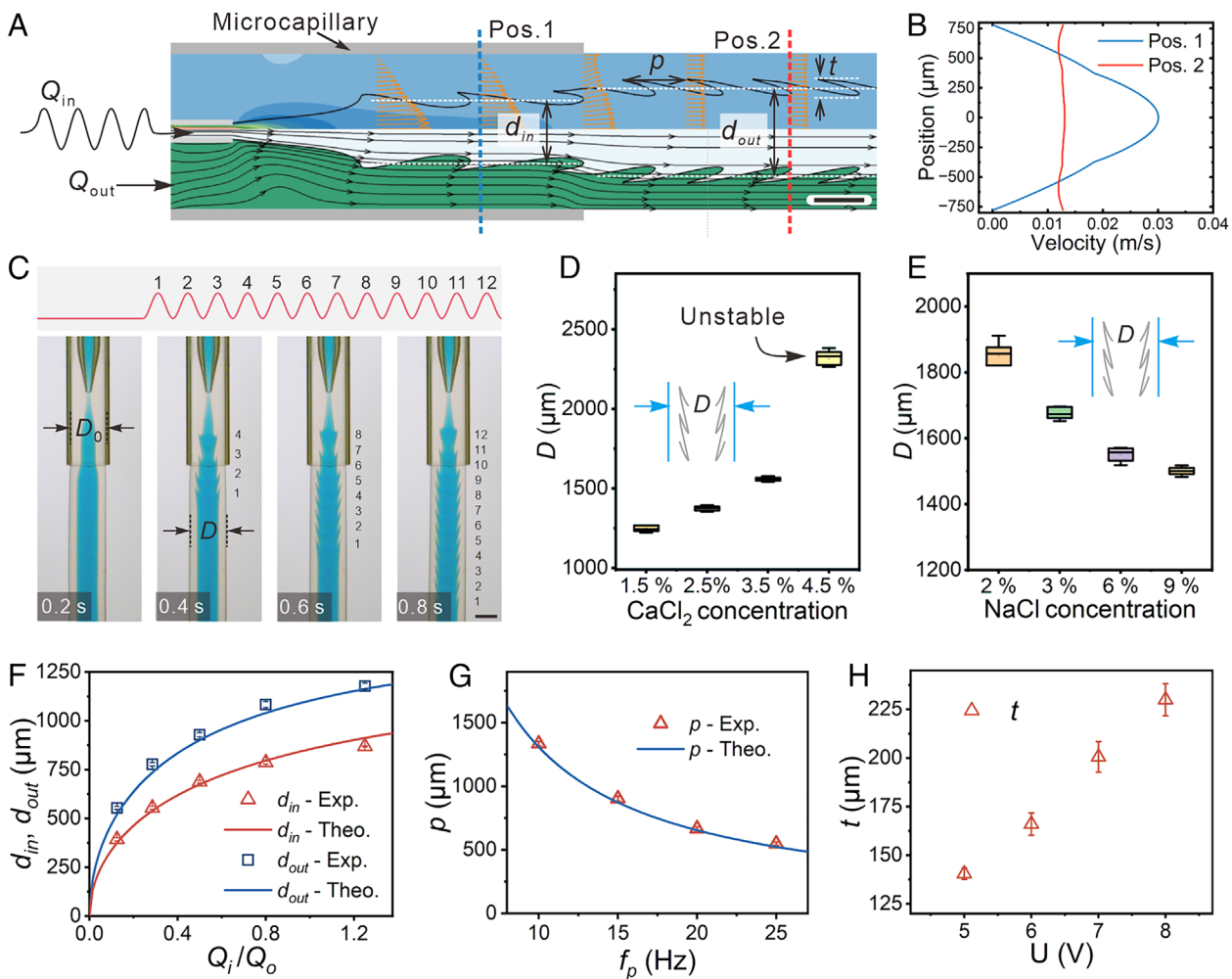


**Fig. 2.** Generation of the corrugated liquid stream from piezoelectric microfluidics. (A) Computational fluid dynamics (CFD) simulation of a vibrated flow stream. The top half shows the cross-section flow radial velocity, and the bottom half shows the streamline diagram; (B) typical velocity profiles in the channel (Pos. 1) and collection phase (Pos. 2) obtained from CFD simulations; (C) high-speed snapshots of the stream morphology in response to the programmable vibrations. The initial 0.2 s corresponds to a stable flow state without vibration. Following this, vibrations are introduced from 0.2 s to 0.8 s, with 12 pulses at a frequency of 20 Hz, aligning with the evolution of 12 corrugations downstream; (D and E) relationship between  $D$  and the ( $D$ ) collection solution concentration or (E) core stream solution concentration; (F) plot of  $d_{in}$  and  $d_{out}$  as a function of  $Q_i/Q_o$ ; (G) plot of  $p$  as a function of  $f_p$ ; (H) plot of  $t$  as a function of  $U$ . [The scale bars are 500  $\mu\text{m}$  in (A) and 1,000  $\mu\text{m}$  in (C).]

Thus, by tuning the piezoelectric microfluidic parameters, the configuration of the core streams can be well controlled (*SI Appendix*, Fig. S6). Our experimental results are consistent with the theoretical predictions, as plotted in Fig. 2 F and G. Moreover, the corrugation thickness  $t$  (in the collection solution) can be adjusted by the piezoelectric voltage  $U$ , as plotted in Fig. 2H.

We then use an ultraviolet (UV) light to further cross-link the sheath stream (*SI Appendix*, Fig. S2), by which hollow microtubes are fabricated with a smooth outer surface. The core stream serves as a sacrificed layer, leaving the inner wall of the tube an inverse structure of the corrugations, as shown in Fig. 3 A and B. Moreover, benefiting from the continuous spinning process in microfluidics, large-scale generation of these microtubes is easily achieved with a typical production speed of  $\sim 1.3 \text{ cm/s}$  (under the typical flow conditions of  $Q_i = 30 \text{ mL/h}$  and  $Q_o = 60 \text{ mL/h}$ ), as shown in Fig. 3 C and D. The microstructure of the microtubes is characterized by a laser scanning confocal microscope, as shown in Fig. 3 E and F. Since the configuration parameters, i.e.,  $d$ ,  $p$ , and  $t$  of the core stream are adjustable, the shape parameters of the microtubes, including  $d$ ,  $p$ ,  $t$  (depicted in Fig. 3A) are also adjustable accordingly (*SI Appendix*, Fig. S7). We then use a scanning electron microscope (SEM) to characterize the microstructure

feature of the microtube. As shown in Fig. 3 G–I, the microtube maintains truncated cone-shaped chambers stacked along the axial direction in its dehydrated state after natural drying. We observed that the hydrated microtubes can achieve a tensile strain up to 15.3%, whereas the dehydrated microtube can extend to a tensile strain up to 55.5% (*SI Appendix*, Fig. S8). The dehydrated tube can swell and rehydrate upon immersion in water, returning to its predehydration state in about 7 min (*SI Appendix*, Fig. S9). Notably, the liquid-diode microtube is created highly flexible benefiting from the rational choice of the material component—the dual-network hydrogel formed by PEGDA and calcium alginate. Because PEGDA serves as the primary component, the microtube can maintain morphological stability even when immersed in saturated NaCl solution for 2 wk (*SI Appendix*, Fig. S10). Based on this, we can easily shape the microtubes into various graphic patterns by bending, twisting, and knotting, with curvature radii down to  $\sim 1.03 \text{ mm}$  without damaging the tube's inner structure (Fig. 3 J–L).

The asymmetric structural feature of the inner wall of the microtube facilitates directional liquid transport, as shown in Fig. 4A. When water is continuously injected into the microtube at a constant flow rate (30  $\mu\text{L/min}$ ), it initially moves toward the narrow

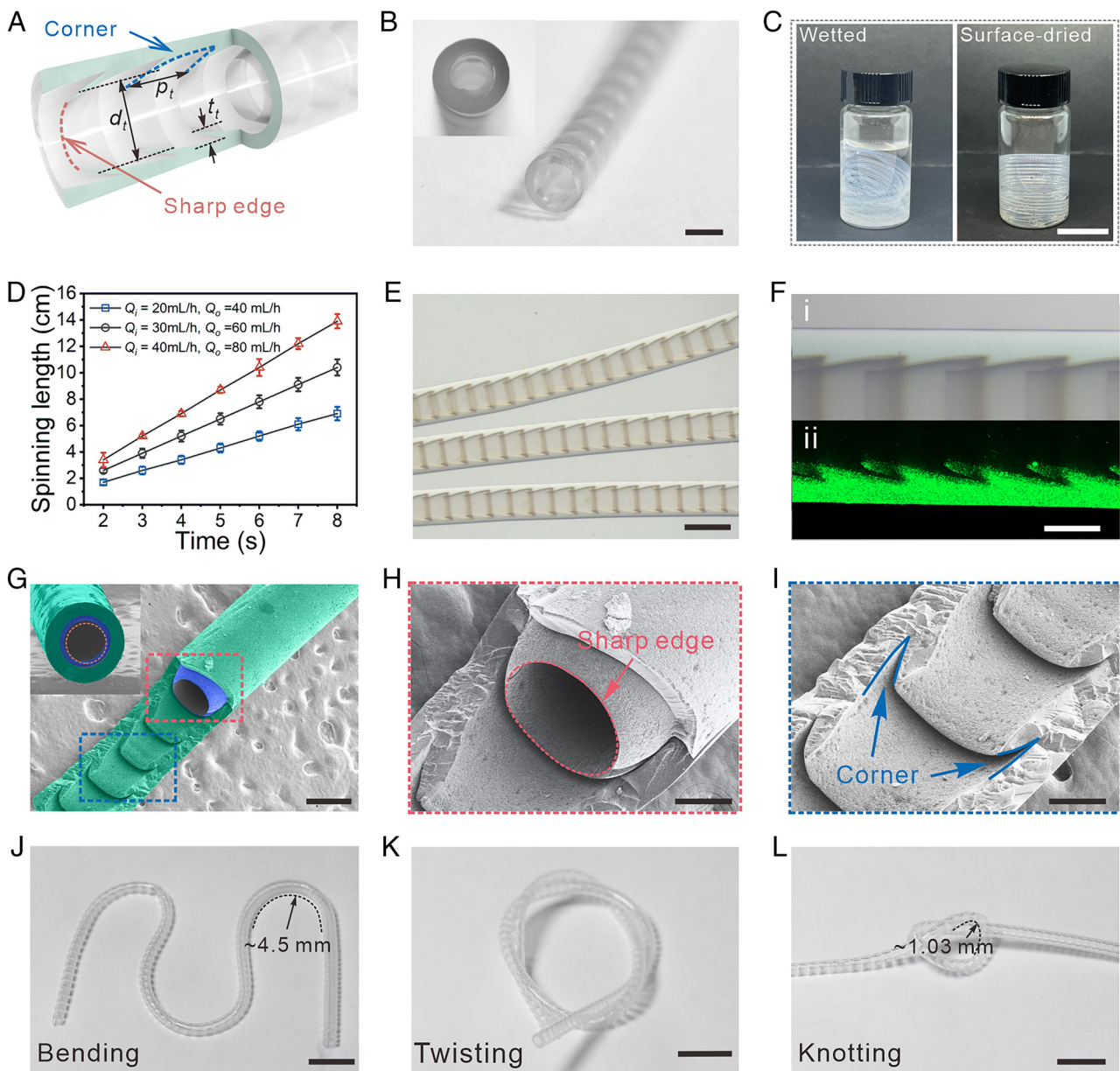


**Fig. 3.** Characterization of the microtubes. (A) Schematic illustration of the structure of the microtube; (B) optical images of one microtube; (C) a batch of hemline microfibers ( $\sim 2.4 \text{ m}$ ) collected in wetted state and surface-dried state after removal of surface and interior water; (D) the production speed of the microtubes at different flow rate conditions; (E) magnification of the collected fibers; (F) detailed view of the microtube: (i) bright-field microscopic and (ii) CLSM images of the microtube; (G–I) SEM images showing the microstructure of the microtube; (J–L) the flexible microtube can be shaped by (J) bending, (K) twisting, and (L) knotting. [Scale bars are 1 mm in (B), 2 cm in (C), 500  $\mu\text{m}$  in (F) and (G), 2 mm in (E), 200  $\mu\text{m}$  in (H) and (I), and 5 mm in (J–L).]

end of the cone and reaches the sharp edge (defined as the backward direction); once contacting the edge (approximately moving by one pitch distance), it becomes pinned, as shown in Fig. 4B. Subsequently, the water stream continues to transport in the opposite direction (defined as the forward direction) and moves approximately 16 mm in 24 s (under specific geometric parameter conditions shown in Fig. 4C and Movie S2). The mechanism of such directional transport can be explained as follows: At the initial stage, two distinct liquid menisci form at the ends of the truncated cone, corresponding to two radii  $r_0 < r_2$  (SI Appendix, Fig. S19A and Note S3). This induces a Laplace pressure gradient ( $p_0 > p_2$ ), driving water to move toward the narrow end (23, 24, 52). Once the liquid interface reaches the narrow end, it becomes pinned at that sharp edge (53), as illustrated in Fig. 4D and SI Appendix, Fig. S19B. Moreover, the dehydrated tube enables unidirectional transport and remains reusable even after reswelling to its hydrated

state (SI Appendix, Fig. S11). For detailed analysis, we capture the process of liquid transport (Movie S3) and measure the periodic variations in the radius of curvature at the pinning position. We find that, as the liquid injection continues, the radius of liquid curvature at the pinned location continues to increase, leading to decrease of the Laplace pressure at the pinning interface until below the forward pressure ( $p_1 < p_2$ ), as illustrated in Fig. 4E. As a result, the liquid begins to transport in the forward direction. During forward transport, the corner structure facilitates rapid filling of the microcavity due to capillary rise, thereby reducing the liquid pressure at the pinned location (Fig. 4F and G and SI Appendix, Fig. S12 and Movie S4).

Based on these mechanisms, the microtube enables continuous directional liquid transport, i.e., acting as liquid diodes. Such directional transport behavior is notably distinct from microtubes with a smooth inner wall, which shows the transport properties

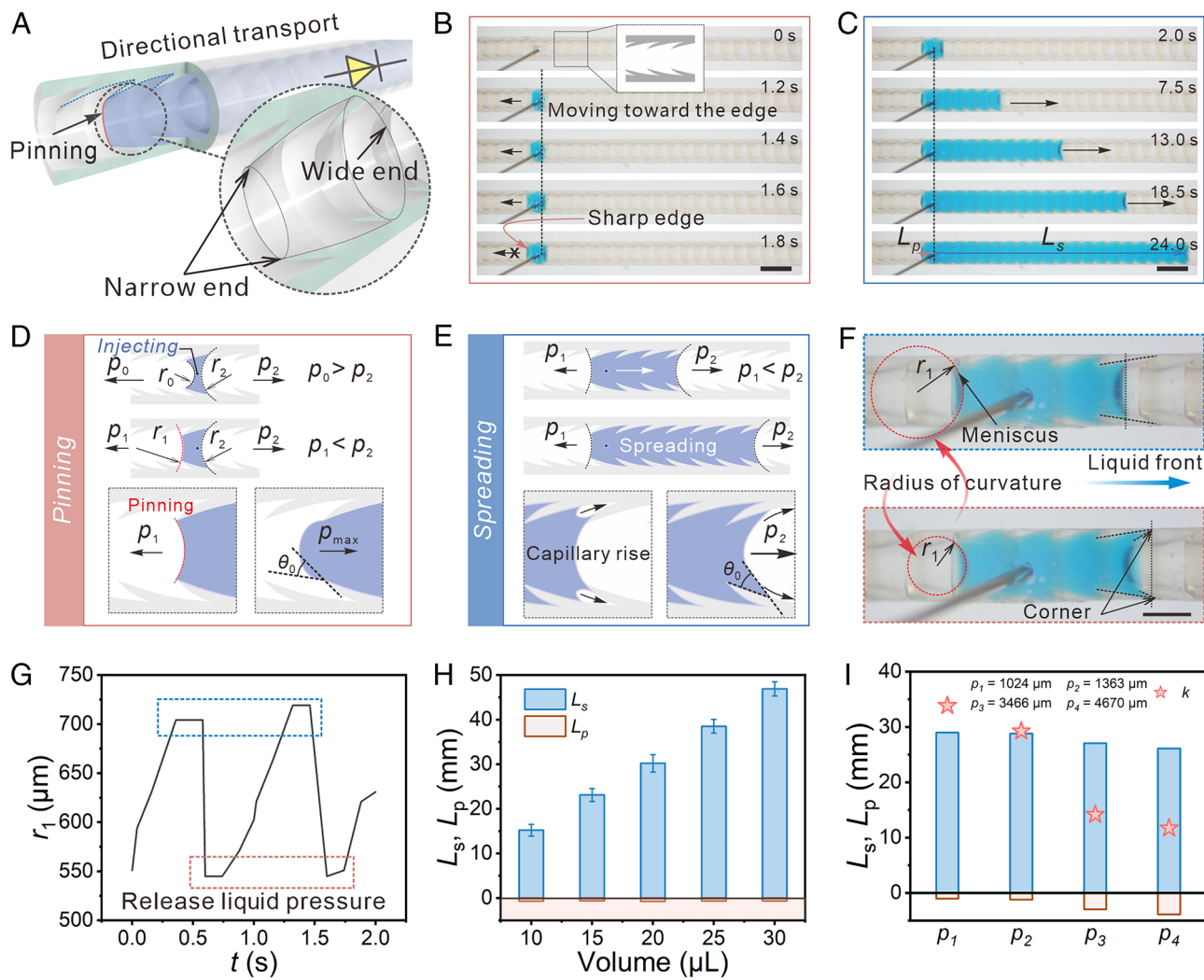


**Fig. 4.** Liquid transport within the liquid-diode microtube. (A) Schematic of the structural features of the microtube and the directional liquid transport behavior; (B) the initial stage of the backward liquid transport by approximately one pitch distance and the pinning effect at the sharp edge; (C) the continuous directional spreading stage due to the Laplace pressure gradient.  $p_t = 870 \mu\text{m}$ ,  $d_t = 910 \mu\text{m}$ , the injection flow rate is  $30 \mu\text{L}/\text{min}$ ; (D) schematic of the mechanism of the initial backward transport and pinning at the sharp edge. As the pressure of the injected fluid increases, the liquid surface at the pinning location can transit from a concave meniscus to a convex meniscus.  $\theta_0$  represents the static contact angle of the liquid on the wall and  $p_{\max}$  stands for the maximum Laplace pressure at the pinning location; (E) schematic of the mechanism of the forward transport and the capillary rise effect, the blue dots represent the injection position; (F) corner-induced capillary rise leads to periodic variations in the curvature radius of the liquid at the pinned sharp edge location; (G) evolution of the radius of curvature at the pinning position; (H) plot of  $L_s$  and  $L_p$  versus the injection volume; (I) plot of  $L_s$  and  $L_p$  versus the corrugation pitch of the microtube (injection volume:  $20 \mu\text{L}$ ). [Scale bars are 2 mm in (B and C), and 1 mm in (F).]

in both directions (*SI Appendix*, Fig. S13). To ensure directional transport within the tube, it is essential to remove water from the corners to expose the sharp edge; otherwise, bidirectional transport would occur (*SI Appendix*, Fig. S14). In addition, we find that the direction of liquid transport is unaffected by the injection direction, but depends solely on the tube's structure (*SI Appendix*, Fig. S15). For a microtube with given structural parameters, the transport distance is determined by the injected liquid volume (Fig. 4H). Furthermore, we define a diode coefficient,  $k = L_s/L_p$ , where  $L_s$  and  $L_p$  refers to the liquid transport distance at the forward and backward direction, respectively. We find that when the injected liquid volume is held constant, the corrugation pitch of the microtube inner wall influences the value of  $k$  (Fig. 4I). This is because at the initial stage, the liquid tends to move backward toward the nearest sharp edge (*SI Appendix*, Fig. S16). By continuing the liquid injection process,  $L_s$  will increase while  $L_p$  keeps unchanged. This will increase  $k$  and diminish the impact of the pitch. The directional liquid transport in closed diode-like microtubules is also applicable to various liquids (*SI Appendix*, Fig. S17).

Taken together, the microtubes with designed asymmetric microstructures possess liquid directional transport ability and exhibit excellent liquid diode properties.

The microtubes exhibit remarkable flexibility and liquid-diode property, enabling the creation of fluid pathways of various configurations, antigravity capabilities, and long-distance directional water transport, as demonstrated in *Movie S5*. For a specific microtube (with parameters approximately  $\alpha = 14.6^\circ$ ,  $\beta = 60^\circ$ ,  $R_1 = 400 \mu\text{m}$ , and  $d_t \approx 900 \mu\text{m}$ ), the sharp edge can maintain a maximum pressure of approximately  $342 \text{ Pa}$ . Directional transport can be achieved as long as the condition below is satisfied (for further details, please refer to *SI Appendix*, Notes S4).

$$\frac{128 * 3.3 \mu\text{L} Q_{\text{inject}}}{\pi d_t^4} + \rho g h < \frac{2\gamma \cos(\beta - \theta_0)}{R_1} + \frac{2\gamma \cos(\alpha + \theta_0)}{R_{\text{front}}} \quad [3]$$

Specifically, these microtube liquid diodes can be easily shaped in a plane. When water is introduced at one end, it propagates

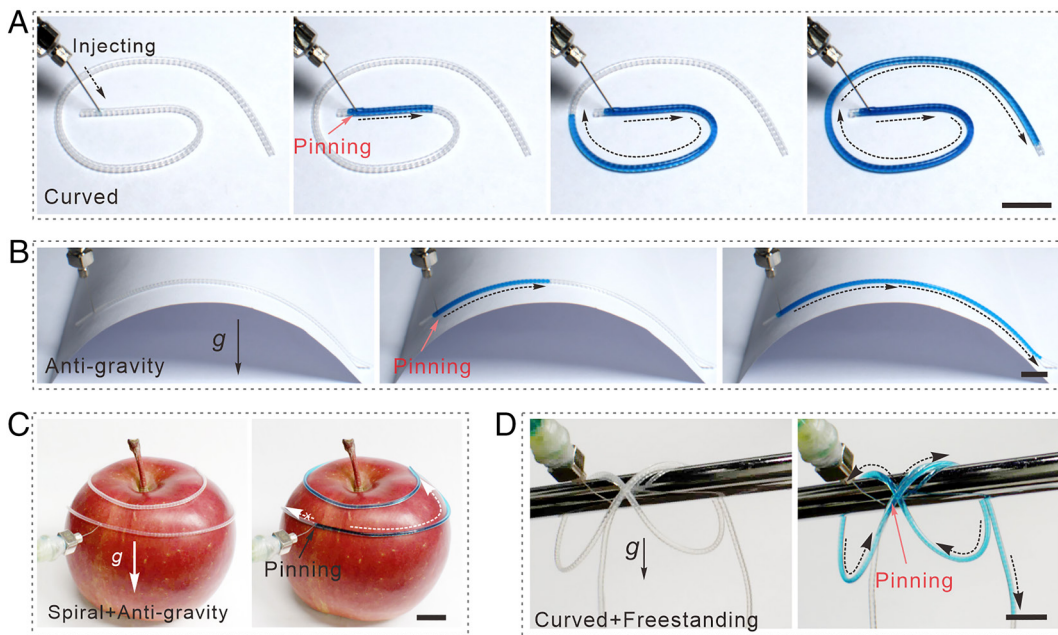


**Fig. 5.** Directional liquid transport along arbitrary paths in the microtube liquid diode. (A) The microtube is contoured to a predesignated curved pattern to direct liquid flow; (B) antigravity liquid transport on an arched surface; (C) liquid transport at an apple surface; (D) liquid transport in a knotted microfluidic channel formed by arbitrarily dangling the microtube. (Scale bars are 1 cm.)

in a specific direction along the tube (Fig. 5A). In addition to planar bending, the tubes can be seamlessly arranged on curved surfaces and conduct antigravity liquid transport. In a simple experiment, we place a tube on an arch surface and inject liquid at one end. We find that the tube can retain its unidirectional liquid transport capacity; the liquid climbs up over the highest point and continues to travel in the tube for a long distance (Fig. 5B). The ability of liquid transport along curved surfaces is further validated in daily life scenarios, as shown in a helical-ascent path on the surface of an apple (Fig. 5C). Moreover, the microtubes can be coiled along a cylinder or arbitrarily hung, either in contact with a surface or in a free-standing configuration (Fig. 5D and *SI Appendix*, Fig. S18). The versatile design of fluidic channel configurations can pave the way for constructing different micromixers. These results demonstrate the remarkable flexibility of the liquid-diode microtube, making it suitable for a wide range of applications.

In addition to the flexibility, another important feature of the liquid-diode microtube is that the liquid transport takes place in a closed space. Thus, the liquid diodes can serve as basic components to construct circuit-like devices. To this end, we prepare short microtube segments with determined lengths. Instead of continuous spinning, we adopt a flow lithography strategy. As shown in Fig. 6A, a photomask is used to control the UV exposure of the core-sheath stream in the microfluidic system. By consecutive polymerization, discrete microtube segments can be produced (Fig. 6B). Additionally, by programming the UV illuminating signal, the length of the liquid diodes can also be tailored (Fig. 6 C and D). These short liquid diodes closely resemble electronic diode components that can be integrated into circuits. As a proof-of-concept, we make a PDMS microfluidic device with four fluidic channels, each embedded with one liquid diode segment oriented at defined directions. We then connected the fluidic channels to four light-emitting diodes (LEDs) using wires on a breadboard and constructed a fluidic-electric circuit. (Fig. 6E). As shown in Fig. 6F, conduction occurs only when both the liquid diode and light-emitting diode are in the forward-biased state. Given the flexibility and programmability of

the liquid diode segments, this approach offers inspiration for more complex logic operations.

## Discussion

In summary, we have presented a type of flexible liquid-diode microtube created through a piezoelectric microfluidic platform. These microtubes are formed by pulsating a core sacrificial jet and curing a surrounding sheath stream. This results in an asymmetric inner wall of the microtube with overlapped truncated cone-shaped cavities, each presenting a sharp edge and corner along the axial direction. Precise control over the structural features is achieved by adjusting the microfluidic and piezoelectric operation parameters. The unique structure makes the microtubes liquid diodes, allowing for directional liquid transport within confined spaces due to Laplace gradient and asymmetric pinning effect. The continuous fabrication of the microtubes, provided by microfluidics, enables long-distance liquid transport; the flexibility of the microtubes, owing to the rational choice of the component material, facilitates liquid transport along arbitrary pathways. Apart from long-length tubes, short-length tubes are prepared through flow lithography. Such liquid diode segments can serve as fundamental components in a fluidic-electronic circuit capable of executing logic operations, potentially paving the way for advancements in wearable technology, especially in health monitoring or sweat sensing. The above results indicate the multifunction of the liquid diodes. Future efforts can focus on incorporating stimuli-responsive nanoparticles or utilizing stimuli-responsive materials in the outer phase, potentially allowing these liquid diodes to possess active switching or pumping capabilities. For the fabrication platform, the dynamic flow control system can be integrated with advanced lithography technique or multichannel design of the microfluidic device to achieve multicomponent tubes with multifunctional properties. Additionally, combination of the piezoelectric microfluidic spinning platform with 3D printing may lead to the creation of macroscale entangled tube networks in various 3D shapes, thereby expanding their applications in real-world scenarios.

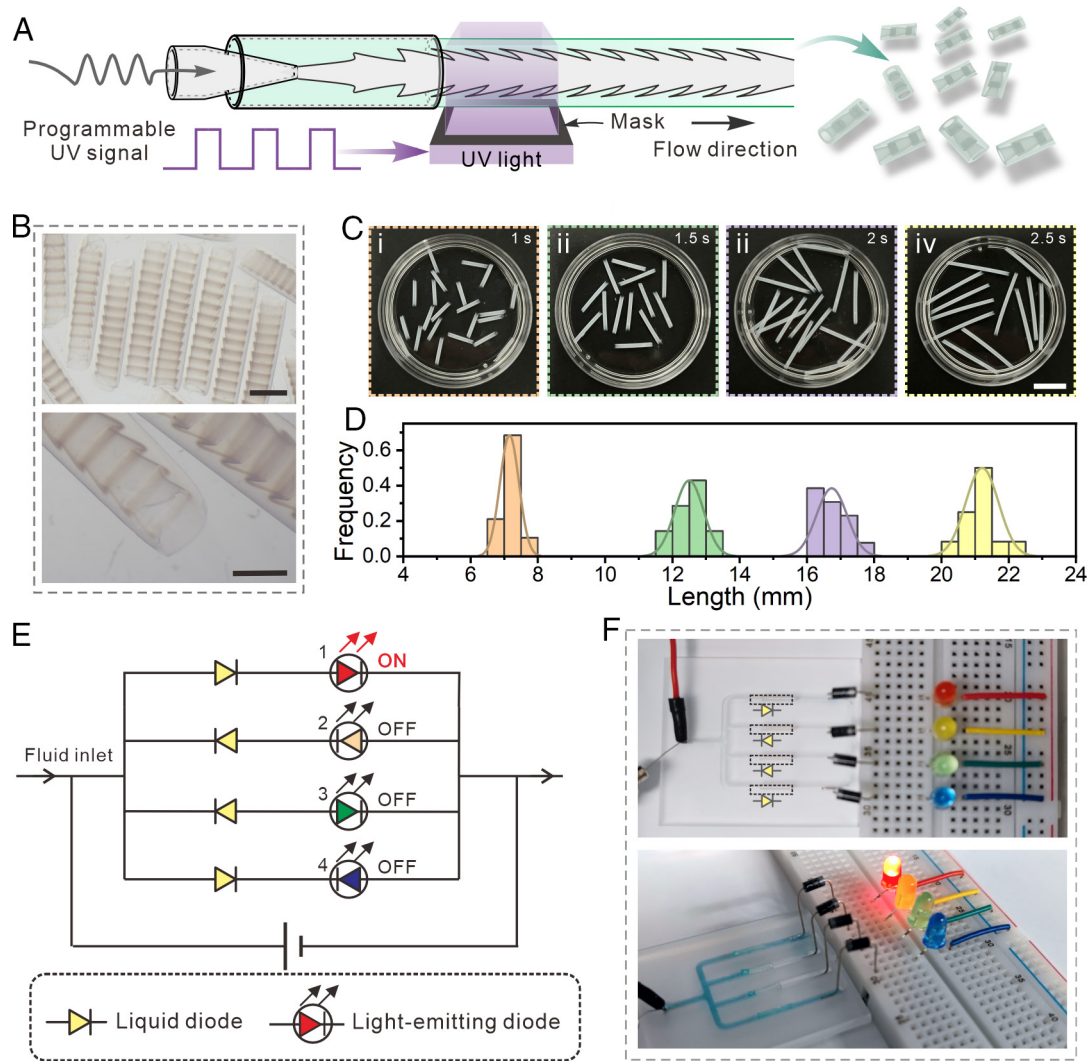


**Fig. 6.** Preparation of short liquid diodes and the construction of a fluidic-electric circuit device. (A) Illustration of the creation of short liquid diodes through programmable control of UV exposure, aided by a mask (0.5 mm). (B) microscope photographs of the liquid-diode segments; (C and D) short liquid diodes with different lengths; (E and F) schematic and photograph of the fluidic-electric circuit. Conduction occurs only when both the liquid diode and light-emitting diode are in the forward-biased state. The injected liquid is a conductive NaCl solution. [Scale bars are 2 mm in the Top panel of (B), 1 mm in the Bottom panel of (B), and 1 cm in (C).]

## Materials and Methods

**Materials.** PEG-diacylate (PEGDA, Mn = 700), 2-hydroxy-2-methylphenylpropane (HMPP), and polyvinyl alcohol (PVA, Mn = 13,000 ~ 23,000) were sourced from Sigma Aldrich. Alfa Aesar provided sodium alginate with extremely low viscosity, while Maclin supplied calcium chloride. Invitrogen supplied fluorescent polystyrene (PS) nanoparticles (F8811). Ultrapure water with a resistivity of 18.2 MΩ·cm was obtained using a Millipore Milli-Q system. PEGDA is employed to enhance the mechanical robustness of the tubes. Sodium alginate facilitates rapid ionic cross-linking at the outlet. PVA is utilized to tune the viscosity of the inner phase to match that of the outer phase. By altering the salinity of both the inner phase and collection solutions, the density of the inner phase and collection solution can be matched with that of the outer phase, thereby enabling the modulation of the external diameter of the microtube. In the typical experiment, the inner phase consisted of 5% PVA and 6% NaCl (1.045 g/cm<sup>3</sup>), and the outer phase was a mixture of 0.5% sodium alginate with 20% PEGDA and 1.25% HMPP (1.039 g/cm<sup>3</sup>). The collection solution used was a 3.5% CaCl<sub>2</sub> solution (1.025 g/cm<sup>3</sup>).

**Piezoelectric Microfluidic System.** The construction of a capillary microfluidic device involves coaxially aligning two cylindrical capillaries on a glass slide. One cylindrical capillary, with an inner and outer diameter of 580 μm and 1.0 mm (World Precision Instruments), is tapered and polished to a 200 μm inner diameter tip using a capillary puller (Sutter Instrument, P-97) and a microforge (Narishige, MF-830) to

serve as the injection tube. The other cylindrical capillary, with an inner diameter of 1,560 μm, functions as the collection tube. These two capillaries are aligned, with the distance from the tip to the exit set at 3 mm (SI Appendix, Fig. S1). To prevent polymerization of the photocurable material in the chip, the entire chip including the connected tubing and the chip's outlet is wrapped by black tapes. Additionally, during the tube preparation process, the UV light beam is positioned about 1 mm below the outlet. Transparent epoxy resin seals the joints of these capillaries as needed.

A piezoelectric stack is employed to transmit programmable vibration through contact with a thin Polytetrafluoroethylene (PTFE) membrane that holds the inner fluid. Connected to a signal generator (Siglent, SDG 2000X) via a power amplifier (Core morrow, E-05), the piezoelectric stack allows control over amplitude and frequency. Unless stated otherwise, the power amplifier magnification is set to 12x, and voltage values throughout this paper are represented as  $V_{pp}$  (peak-to-peak) of the signal generator. The setup is immersed in a 3.5% CaCl<sub>2</sub> solution. To fabricate long tubes, a deep collecting container is required. The setup includes an UV light head (365 nm, EXFO OmniCure SERIES 1000, 365 nm, 100 W) positioned below the exit of the collection tube to facilitate immediate curing of the liquids flowing out from the chip. For the generation of liquid diode segments, we employ a mask with a window length of 0.5 mm.

**Characterizations on the Hemline Jet/Microfiber.** The flow dynamics of the streams is monitored by a high-speed camera (Phantom, VEO E-310L) with a microscope. The fluorescence image of the prepared microtubes is observed by a laser

scanning confocal microscope (LSCM, Nikon, A1). The microstructures of the solidified microtubes are captured by a scanning electron microscope (SEM, HITACHI, SU8010).

**Tracking the Liquid Transport Dynamics.** The as-prepared liquid diode tubes undergo a thorough washing process, involving five cycles to remove the inner sacrificed solution. Subsequently, nitrogen gas and absorbent paper are employed to effectively remove the water in the interior of the tube. We capture the transport behaviors of dyed water at room temperature with a CCD camera. Typically, water is pumped through a stainless needle with a certain flow rate (30  $\mu$ L/min) using a syringe pump (LSP01-2A, Longer). To observe the transport dynamics of water in the corner, we monitor the moving boundary of water with a high-speed camera (Phantom, VEO E-310L) from the front view.

**Construction of the Fluidic-Electric Circuit Device.** A PDMS microfluidic chip is fabricated using a 3D-printed mold. Subsequently, the channels are treated with a plasma instrument to enhance wall hydrophilicity, facilitating

fluid flow. The channel has a width of 1.6 mm and a semicircular bottom designed to match the fluidic diode's shape. A shared fluid injection point connects the four channels. We then carefully place liquid diode segments into their designated channels according to the preestablished design, followed by circuit connection. Saturated sodium chloride solution is employed and injected at the inlet, flowing through the forward-biased liquid diode and activating the forward-biased LED.

**Data, Materials, and Software Availability.** All study data are included in the article and/or [supporting information](#).

**ACKNOWLEDGMENTS.** This work was supported by the National Natural Science Foundation of China (T2225003, 22202050, 32271383, and 52073060), the National Key Research and Development Program of China (2020YFA0908200), and the CUHK Direct Grant (4055219).

1. Y.-H. Kim *et al.*, Chiral-induced spin selectivity enables a room-temperature spin light-emitting diode. *Science* **371**, 1129–1133 (2021).
2. F. Ando *et al.*, Observation of superconducting diode effect. *Nature* **584**, 373–376 (2020).
3. M. Smith, V. Cacucciolo, H. Shea, Fiber pumps for wearable fluidic systems. *Science* **379**, 1327–1332 (2023).
4. S. Feng *et al.*, Three-dimensional capillary ratchet-induced liquid directional steering. *Science* **373**, 1344–1348 (2021).
5. N. A. Dudukovic *et al.*, Cellular fluidics. *Nature* **595**, 58–65 (2021).
6. H. Dai, Z. Dong, L. Jiang, Directional liquid dynamics of interfaces with superwettability. *Sci. Adv.* **6**, eabb5528 (2020).
7. M. Sun *et al.*, Exploiting ferrofluidic wetting for miniature soft machines. *Nat. Commun.* **13**, 7919 (2022).
8. H. Patel *et al.*, Design of medical tympanostomy conduits with selective fluid transport properties. *Sci. Transl. Med.* **15**, eadd9779 (2023).
9. K.-C. Park *et al.*, Condensation on slippery asymmetric bumps. *Nature* **531**, 78–82 (2016).
10. G. Lagubeau, M. Le Merre, C. Clanet, D. Quéré, Leidenfrost on a ratchet. *Nat. Phys.* **7**, 395–398 (2011).
11. V. Cacucciolo *et al.*, Stretchable pumps for soft machines. *Nature* **572**, 516–519 (2019).
12. A. Li *et al.*, Programmable droplet manipulation by a magnetic-actuated robot. *Sci. Adv.* **6**, eaay5808 (2020).
13. M. K. Chaudhury, G. M. Whitesides, How to make water run uphill. *Science* **256**, 1539–1541 (1992).
14. S. Daniel, M. K. Chaudhury, J. C. Chen, Fast drop movements resulting from the phase change on a gradient surface. *Science* **291**, 633–636 (2001).
15. R. W. Style *et al.*, Patterning droplets with durotaxis. *Proc. Natl. Acad. Sci. U.S.A.* **110**, 12541–12544 (2013).
16. K.-H. Chu, R. Xiao, E. N. Wang, Uni-directional liquid spreading on asymmetric nanostructured surfaces. *Nat. Mater.* **9**, 413–417 (2010).
17. A. R. Parker, C. R. Lawrence, Water capture by a desert beetle. *Nature* **414**, 33–34 (2001).
18. Y. Cui, D. Li, H. Bai, Bioinspired smart materials for directional liquid transport. *Ind. Eng. Chem. Res.* **56**, 4887–4897 (2017).
19. J. Li *et al.*, Topological liquid diode. *Sci. Adv.* **3**, eaao3530 (2017).
20. C. Duprat, S. Protiere, A. Beebe, H. A. Stone, Wetting of flexible fibre arrays. *Nature* **482**, 510–513 (2012).
21. W. Xu *et al.*, Triboelectric wetting for continuous droplet transport. *Sci. Adv.* **8**, eade2085 (2022).
22. J. Ju *et al.*, A multi-structural and multi-functional integrated fog collection system in cactus. *Nat. Commun.* **3**, 1247 (2012).
23. J.-A. Lv *et al.*, Photocontrol of fluid slugs in liquid crystal polymer microactuators. *Nature* **537**, 179–184 (2016).
24. M. Prakash, D. Quéré, J. W. Bush, Surface tension transport of prey by feeding shorebirds: The capillary ratchet. *Science* **320**, 931–934 (2008).
25. C. Yang, Y. Yu, L. Shang, Y. Zhao, Flexible hemline-shaped microfibers for liquid transport. *Nat. Chem. Eng.* **1**, 87–96 (2024).
26. C. Gabbard, J. Bostwick, Surface-engineered microfibers provide liquid transport flexibility. *Nat. Chem. Eng.* **1**, 31–32 (2024).
27. H. Chen *et al.*, Continuous directional water transport on the peristome surface of *Nepenthes alata*. *Nature* **532**, 85–89 (2016).
28. Y. Zheng *et al.*, Directional water collection on wetted spider silk. *Nature* **463**, 640–643 (2010).
29. L. Wu *et al.*, Highly efficient three-dimensional solar evaporator for high salinity desalination by localized crystallization. *Nat. Commun.* **11**, 521 (2020).
30. Y. Tian *et al.*, Large-scale water collection of bioinspired cavity-microfibers. *Nat. Commun.* **8**, 1080 (2017).
31. X. Liu, B. Li, Z. Gu, K. Zhou, 4D printing of butterfly scale-inspired structures for wide-angle directional liquid transport. *Small* **19**, 2207640 (2023).
32. J. Li *et al.*, Nature-inspired reentrant surfaces. *Prog. Mater. Sci.* **133**, 101064 (2022).
33. C. Li *et al.*, Bioinspired inner microstructured tube controlled capillary rise. *Proc. Natl. Acad. Sci. U.S.A.* **116**, 12704–12709 (2019).
34. Y. Liu *et al.*, Excellent liquid unidirectional transport inner tilted-sector arrayed tubes. *Adv. Mater. Interfaces* **10**, 2300239 (2023).
35. J. Li *et al.*, Flexible topological liquid diode catheter. *Mater. Today Phys.* **12**, 100170 (2020).
36. G. M. Whitesides, The origins and the future of microfluidics. *Nature* **442**, 368–373 (2006).
37. A. S. Utada *et al.*, Monodisperse double emulsions generated from a microcapillary device. *Science* **308**, 537–541 (2005).
38. Y. Chao, H. C. Shum, Emerging aqueous two-phase systems: From fundamentals of interfaces to biomedical applications. *Chem. Soc. Rev.* **49**, 114–142 (2020).
39. S. Battat, D. A. Weitz, G. M. Whitesides, An outlook on microfluidics: The promise and the challenge. *Lab Chip* **22**, 530–536 (2022).
40. C. Yang, Y. Yu, X. Wang, L. Shang, Y. Zhao, Programmable knot microfibers from piezoelectric microfluidics. *Small* **18**, 2104309 (2022).
41. C. Yang *et al.*, Bioinspired stimuli-responsive spindle-knotted fibers for droplet manipulation. *Chem. Eng. J.* **451**, 138669 (2023).
42. L. Shang, Y. Cheng, Y. Zhao, Emerging droplet microfluidics. *Chem. Rev.* **117**, 7964–8040 (2017).
43. H. Chen, J. Guo, F. Bian, Y. Zhao, Microfluidic technologies for cell deformability cytometry. *Smart Med.* **1**, e20220001 (2022).
44. Y. Yu *et al.*, Bioinspired helical microfibers from microfluidics. *Adv. Mater.* **29**, 1605765 (2017).
45. L. Shang *et al.*, Bioinspired multifunctional spindle-knotted microfibers from microfluidics. *Small* **13**, 1600286 (2017).
46. Y. Liu *et al.*, Water harvesting of bioinspired microfibers with rough spindle-knots from microfluidics. *Small* **16**, 1901819 (2020).
47. S. Wang *et al.*, Bioinspired robust helical-groove spindle-knot microfibers for large-scale water collection. *Adv. Funct. Mater.* **33**, 2305244 (2023).
48. P. Zhu, L. Wang, Microfluidics-enabled soft manufacture of materials with tailorable wettability. *Chem. Rev.* **122**, 7010–7060 (2021).
49. Y. Yu, L. Shang, J. Guo, J. Wang, Y. Zhao, Design of capillary microfluidics for spinning cell-laden microfibers. *Nat. Protoc.* **13**, 2557–2579 (2018).
50. A. Sauret, H. C. Shum, Beating the jetting regime. *Int. J. Nonlinear Sci. Numer. Simul.* **13**, 351–362 (2012).
51. Z. Zhu, T. Si, R. X. Xu, Microencapsulation of indocyanine green for potential applications in image-guided drug delivery. *Lab Chip* **15**, 646–649 (2015).
52. Exstrand, Retention forces of a liquid slug in a rough capillary tube with symmetric or asymmetric features. *Langmuir* **23**, 1867–1871 (2007).
53. J. Oliver, C. Huh, S. Mason, Resistance to spreading of liquids by sharp edges. *J. Colloid Interface Sci.* **59**, 568–581 (1977).